



Cite this: *Phys. Chem. Chem. Phys.*,
2016, 18, 32418

Oxygen vacancy promoted methane partial oxidation over iron oxide oxygen carriers in the chemical looping process

Zhuo Cheng,^a Lang Qin,^a Mengqing Guo,^a Mingyuan Xu,^a Jonathan A. Fan^b and Liang-Shih Fan^{*a}

We perform *ab initio* DFT+*U* calculations and experimental studies of the partial oxidation of methane to syngas on iron oxide oxygen carriers to elucidate the role of oxygen vacancies in oxygen carrier reactivity. In particular, we explore the effect of oxygen vacancy concentration on sequential processes of methane dehydrogenation, and oxidation with lattice oxygen. We find that when CH₄ adsorbs onto Fe atop sites without neighboring oxygen vacancies, it dehydrogenates with CH_x radicals remaining on the same site and evolves into CO₂ via the complete oxidation pathway. In the presence of oxygen vacancies, on the other hand, the formed methyl (CH₃) prefers to migrate onto the vacancy site while the H from CH₄ dehydrogenation remains on the original Fe atop site, and evolves into CO via the partial oxidation pathway. The oxygen vacancies created in the oxidation process can be healed by lattice oxygen diffusion from the subsurface to the surface vacancy sites, and it is found that the outward diffusion of lattice oxygen atoms is more favorable than the horizontal diffusion on the same layer. Based on the proposed mechanism and energy profile, we identify the rate-limiting steps of the partial oxidation and complete oxidation pathways. Also, we find that increasing the oxygen vacancy concentration not only lowers the barriers of CH₄ dehydrogenation but also the cleavage energy of Fe–C bonds. However, the barrier of the rate-limiting step cannot further decrease when the oxygen vacancy concentration reaches 2.5%. The fundamental insight into the oxygen vacancy effect on CH₄ oxidation with iron oxide oxygen carriers can help guide the design and development of more efficient oxygen carriers and CLPO processes.

Received 11th September 2016,
Accepted 2nd November 2016

DOI: 10.1039/c6cp06264d

www.rsc.org/pccp

1 Introduction

Chemical looping combustion (CLC) is an innovative technology that can be used for CO₂ capture and enhancement of energy efficiency of the combustion process. Direct contact between fuel and combustion air is avoided in this combustion scheme.^{1,2} The CLC reactors include a fuel reactor where the metal oxide oxygen carriers are reduced by reaction with the carbonaceous feedstock, and an air reactor where the reduced metal oxides are regenerated by re-oxidization with air. This technology has been developed into a chemical looping partial oxidation (CLPO) process for direct syngas production from methane with significant economic attraction compared to the conventional methane reforming method. In the CLPO process, oxygen carriers provide

oxygen to partially oxidize methane in the fuel reactor or the reducer, while undergoing reduction themselves. The reduced oxygen carriers are then regenerated by air in the air reactor and circulated back to the reducer. The CLPO can generate separate streams of a high purity syngas from the reducer, which obviates several downstream processing steps in the reforming operation, yielding a highly efficient process with high economic benefits.^{3,4} Oxygen carriers play an important role in determining the product quality and process efficiency for the CLPO process. During reduction, the oxygen carriers donate the required amount of lattice oxygen for methane partial oxidation and form oxygen vacancies. In the oxidation step, the depleted oxygen carriers are replenished with gas oxygen from air while the oxygen vacancies are healed. Extensive studies have been performed in the design and development of efficient oxygen carriers. Oxygen carriers for CLPO need to possess properties such as high oxygen-carrying capacity, high fuel conversion, good redox reactivity, fast kinetics, good recyclability, long-term stability, high attrition resistance, good heat-carrying capacity, high melting point, resistance to toxicity, and low production cost.

^a Department of Chemical and Biomolecular Engineering, The Ohio State University, 151 W Woodruff Avenue, Columbus, OH 43210, USA. E-mail: fan.1@osu.edu

^b Department of Electrical Engineering, Ginzton Laboratory, Spilker Engineering and Applied Sciences, Stanford University, 348 Via Pueblo Mall, Stanford, CA 94305, USA

In addition, the applications of partial oxidation for chemical production require certain oxygen carrier properties for accurately controlling the product selectivity. Various oxygen carriers have been studied for CLPO applications, such as transition metal oxides of Mn, Co, Ni, Cu and Fe.^{5–10} Among these oxygen carriers, iron oxides are attractive due to their cost benefits and versatility in applications for chemical looping reactions.^{11–13}

Studies on methane partial oxidation in a chemical looping system using iron oxide oxygen carriers have been conducted in recent years. Luo *et al.*¹⁴ reported that the Fe₂O₃-based oxygen carrier can generate syngas at a concentration higher than 90%, balanced by CO₂ and steam, with full fuel conversion. In their unique moving bed reactor configuration, the reactor is designed to operate with minimal carbon deposition and without the use of steam. The feedstock can be methane, biomass, coal, and other types of carbonaceous fuels, and the H₂/CO ratio may vary from 1:1 to 3:1 depending on the feedstock and operating conditions. Jin *et al.*¹⁵ studied the reduction of Fe₂O₃ and evolution of gas products during CH₄ oxidation using TGA-MS under different reaction atmospheres, and reported that the ventilation air will hamper CH₄ oxidation. However, the methane partial oxidation on iron oxide oxygen carriers is still not fully understood due to the complex nature of Fe₂O₃ and limitations in experimentally detecting the dehydrogenated CH_x radicals and intermediates formed during the partial oxidation process using current spectroscopic techniques. Although recently Huang *et al.*¹⁶ performed a DFT study on CH₄ oxidation with iron oxide and proposed a reaction mechanism, they did not include oxygen vacancies in their model study, which have been proved to play an important role in CH₄ dehydrogenation steps.¹⁷ As aforementioned, the oxygen carriers will donate lattice oxygen to the reactant during methane partial oxidation which leads to the formation of oxygen vacancies. The vacancy sites act as initiators for adsorption of molecules in many surface reactions.^{18–22} Therefore, it is important to discern the stability of different oxygen vacancies on the iron oxide surface, and examine their effect on the interaction between methane and oxygen carriers.

DFT+*U* calculations can improve the accuracy of conventional DFT calculations and provide valuable information on the structure of the active sites and the energy of adsorbed species interacting with the surfaces.^{23–25} In addition, detailed reaction pathways can be derived and characterized by the energy profile of the constituent elementary steps.²⁶ There have been a few DFT studies on the Fe₂O₃ structure. Warschkow *et al.*²⁷ built a slab model of the (001) surface of hematite as well as the bulk structure, and found that vacancies are easier to form if they are closer to the outermost layer of surfaces. Wanaguru *et al.*²⁸ modeled hematite nanoribbons, and showed that built-in oxygen vacancies can be produced on the edge. However, these studies only focus on the solid state and have not considered the relative surface reaction. Although the CH₄ dissociation mechanism on various materials has been widely studied,^{29–32} there are few reports on the CH₄ dehydrogenation and oxidation mechanism on iron oxide. The mechanism of methane partial oxidation on iron oxide oxygen carriers with oxygen vacancies remains unknown. It is also not clear as to

how oxygen vacancies affect methane oxidation to syngas by partial oxidation or CO₂ by complete oxidation. This lack of knowledge hampers the design and development of oxygen carriers. Thus, a detailed study of the role of oxygen vacancies in CH₄ partial oxidation and complete oxidation is essential.

In this study, we present a DFT+*U* and thermochemistry analysis of CH₄ oxidation on the α -Fe₂O₃(001) surface with various oxygen vacancies to explore the role of oxygen vacancies and the oxidation mechanism. We also perform experimental Thermogravimetric Analysis (TGA) to examine our DFT+*U* calculations. This study provides insights into the detailed methane partial oxidation and complete oxidation processes that can be useful in guiding the design of more efficient oxygen carriers and the development of the CLPO process.

2 Method

2.1 Computational

The first-principles calculations were performed within the framework of density functional theory (DFT), using the Vienna Ab Initio Simulation Package (VASP).^{33–35} The generalized gradient approximation of Perdew, Burke and Ernzerhof³⁶ (PBE) was used to represent the exchange–correlation energy. The projector-augmented wave (PAW) method,^{37,38} with a 400 eV energy cutoff, was used to describe the wave functions of the atomic cores. The tetrahedron method with Blöchl corrections³⁹ was used to set the partial occupancies for the orbitals. The α -Fe₂O₃(001) surfaces with various terminations were chosen to model the iron oxide slab. An 8 × 8 × 1 Monkhorst-Pack *k*-point mesh was used for surface calculations. The spin restricted method was used for the investigation of the oxygen vacancy formation on the α -Fe₂O₃(001) surface and spin-unrestricted calculations for the study of the CH_x radical (*x* = 0–3) adsorption and oxidation on the α -Fe₂O₃(001) surface, respectively. The on-site Coulomb repulsion amongst the localized 3d electrons is not described very well in a spin-polarized DFT treatment. To consider this Coulomb repulsion explicitly, we used DFT+*U* correction, which consists of combining the DFT with a Hubbard–Hamiltonian term.^{40,41} Huang *et al.* used a linear response technique to derive specific *U* values for all Fe atoms in several slab geometries of α -Fe₂O₃(001) and showed that the *U* value is a key factor in obtaining theoretical results for surface stability that are congruent with the experimental literature results of the α -Fe₂O₃(001) surface structure.⁴² Rollmann *et al.* found that when increasing *U* from 1 eV to 4 eV, it results in improved values for lattice constants and band gaps as well as better agreement with the density of states by experimental IPS spectra. A further increase in *U* cannot achieve a better agreement.⁴³ Therefore, we choose *U* = 4 eV to describe the energy required for adding an extra d electron to the Fe atom. The calculated α -Fe₂O₃ bulk lattice parameters were *a* = *b* = 5.04 Å and *c* = 13.83 Å, in good agreement with the experimental values (*a* = *b* = 5.038 Å and *c* = 13.772 Å).⁴⁴ It also agrees well with the results of Mosey *et al.* that Fe₂O₃ lattice constants obtained from PBE+*U* calculations are slightly higher than the experimental values.⁴⁵

The oxygen vacancy formation energies are calculated based on the following expression:

$$E_f = E_{\text{tot}} - E_V - \frac{1}{2}E_{\text{O}_2} \quad (1)$$

In eqn (1), E_{tot} is the total energy of the stoichiometric surface, E_V is the total energy of the reduced surface with one oxygen vacancy, and E_{O_2} is the total energy of the optimized gas phase O_2 . The adsorption energies of CH_x ($x = 0-3$) radicals on the $\alpha\text{-Fe}_2\text{O}_3(001)$ surface are calculated using the expression as below:

$$E_{\text{ad}} = E_{\text{CH}_x} + E_{\text{surf}} - E_{(\text{CH}_x+\text{surf})} \quad (2)$$

where E_{CH_x} is the energy of the optimized gas phase geometry of CH_x , E_{surf} is the total energy of the respective surface, and $E_{(\text{CH}_x+\text{surf})}$ is the total energy of the slab with adsorbed CH_x . Based on this definition, a more positive E_{ad} corresponds to a more stable configuration.

For CH_4 dehydrogenation and oxidation barrier calculations, the climbing-image nudged elastic band (CI-NEB) method was used.^{46,47} This method enabled the stationary points to be mapped out along the minimum energy paths and identified transition states for each of the diffusion processes. Because these paths were directed by force projection, the energy was not necessarily consistent with the force being optimized; thus, the force-based optimizer was chosen to ensure the convergence of the nudged elastic band algorithm. Based on this model and proposed mechanism cycles above, we can map the energy profile of CH_4 partial oxidation and complete oxidation pathways by the CI-NEB method. However, we need to correct the energy barriers using the thermochemistry model because the reaction temperature in the chemical looping system is usually higher than 700 °C. We previously developed a modified Brønsted–Evans–Polanyi relationship to calculate the activation energy for the elementary steps of metathesis reaction.⁴⁸ Here, we extend this method to calculate the energy barriers for CH_4 oxidation at 1000 °C using the equation below:

$$E_a(T) = E_{a,\text{DFT}} + \alpha(\Delta H_r(T) - \Delta E_{r,\text{DFT}}) \quad (3)$$

where $E_{a,\text{DFT}}$ corresponds to the forward activation energy barrier at 0 K, which is obtained from CI-NEB calculations. $\Delta H_r(T)$ is the reaction enthalpy at finite temperature, which is calculated from the individual enthalpies of the initial state and the final state for the constituent elementary reactions. $\Delta E_{r,\text{DFT}}$ is the difference between the energies of the final state and the initial state at 0 K. The variable α denotes the relative position of the transition state compared to the initial (*i.e.*, $\alpha = 0$) or final (*i.e.* $\alpha = 1$) state of the relevant elementary dissociation reaction. It can be obtained by considering which image in the CI-NEB calculations corresponds to the transition state. When the value of α is close to 0, it corresponds to an initial-like transition state; thus, the activation energy may be maintained at the DFT value. When the value of α is close to 1, it corresponds to a final-like transition state and the activation energy is corrected using eqn (3). To obtain enthalpy, H , at finite temperature T , for all adsorbed species and products, we correct the electronic energy for the zero point energy (ZPE) contribution and temperature variation using C_p . The heat

capacity $C_p = T \left(\frac{\partial S}{\partial T} \right)_p$ can be computed numerically by differentiating the entropy. The vibrational entropy, S_{vib} , can be directly obtained from the vibrational partition function using the DFT-calculated frequencies.

2.2 Experimental

Fe_2O_3 powders were purchased from Fisher Scientific. Fe_2O_3 was treated by ball milling for 24 hours at room temperature. The mixed powders were uniaxially pressed into a pellet with a diameter of 8 mm and a thickness of 2–3 mm. The top surfaces were perpendicular to the pressing direction and parallel to the die surfaces. The samples were heat treated in air at 110 °C for 2 hours to remove volatile impurities using a 2 °C min^{−1} heating rate and then sintered at 1300 °C for 2 h using 2 °C min^{−1} heating and 2 °C min^{−1} cooling rates, respectively. Approximately 45 mg of disaggregated pellet samples were mounted into an alumina crucible and run through ten oxidation–reduction cycles at 1000 °C with a 45 °C min^{−1} ramp rate using a Setaram SETSYS Evolution Thermogravimetric Analyzer (TGA). Oxidation was performed using a 200 ml min^{−1} flow of gas consisting of 50% air balanced with N_2 . The reduction step used a 200 ml min^{−1} flow of gas containing 50% CH_4 balanced with N_2 . The oxidation and reduction steps lasted for 5 minutes each and were alternated with an intermediate 5 minute flushing step using N_2 at 100 ml min^{−1}.

3 Results and discussion

3.1 Surface termination of the iron oxide oxygen carriers

To investigate the oxidation mechanism, the stable iron oxide surface termination under the chemical looping conditions needs to be determined. The Fe_2O_3 bulk is cleaved along the (001) surface. A 15 Å thick vacuum layer was used to separate the surfaces and their images. The use of the periodic models avoids the introduction of edge effects and allows for a more accurate description of surface relaxation. Depending on the cleavage position and the repeat of iron and oxygen atom ordering, three possible terminations can be built: $\text{Fe}_{(s+1)}\text{O}_{(s)}\text{Fe}_{(s-1)}$, $\text{O}_{(s)}\text{Fe}_{(s-1)}\text{Fe}_{(s-2)}$ and $\text{Fe}_{(s-1)}\text{Fe}_{(s-2)}\text{O}_{(s-3)}$ as shown in Fig. 1.

We calculate the surface free energy to compare the stability of these three surface terminations at 1000 °C and 1 atm by the combined DFT+ U and statistical mechanics method. The $\text{Fe}_2\text{O}_3(001)$ surface energy γ at temperature T and pressure p can be written as:

$$\gamma(T, p) = \frac{1}{A} [G(T, p) - N_{\text{Fe}}\mu_{\text{Fe}} - N_{\text{O}}\mu_{\text{O}}] \quad (4)$$

where μ_{Fe} and μ_{O} are the chemical potentials of Fe and O, respectively, and N_{Fe} and N_{O} are the number of Fe atoms and O atoms, respectively. A is the surface area and G is given by:

$$G(T, p) = E_{\text{DFT}} - TS + PV. \quad (5)$$

For a solid slab system, the vibrational entropy S_{vib} is the main contributor. It can be directly obtained from the vibrational

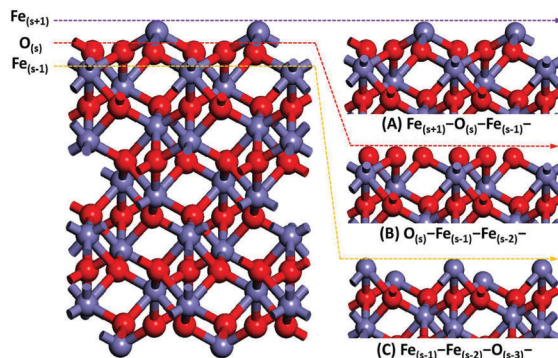


Fig. 1 α -Fe₂O₃(001) surface with different terminations. Iron atoms are displayed as purple balls and lattice oxygen atoms as red balls.

partition function, using the DFT-estimated frequencies ν_i :

$$S_{\text{vib}} = \sum_{i=1}^N \left[\frac{h\nu_i}{T} \frac{X_i}{1 - X_i} - k_B \ln(1 - X_i) \right] \quad (6)$$

where $X_i = \exp(-h\nu_i/k_B T)$.

Fe₂O₃ can be used as the chemical potential reference for Fe as given by:

$$\mu_{\text{Fe}} = \frac{\mu_{\text{Fe}_2\text{O}_3} - 3\mu_{\text{O}}}{2} \quad (7)$$

During the chemical looping process, the oxidation and reduction steps last for 5 minutes each and are alternated with an intermediate 5 minute flushing step using N₂ at 100 ml min⁻¹. Therefore, it can be properly assumed that the surface is in a thermodynamic equilibrium state. It was found that the free energy of the Fe_(s+1)-O_(s)-Fe_(s-1)- terminated surface is 1.24 J m⁻² at 1000 °C and 1 atm, which is lower than the free energies of O_(s)-Fe_(s-1)-Fe_(s-2)- and Fe_(s-1)-Fe_(s-2)-O_(s-3)- terminated surfaces (Table 1⁴⁹). Therefore, Fe_(s+1)-O_(s)-Fe_(s-1)- is the dominant termination surface which also was proven in the X-ray photoelectron diffraction study. Table 1 also shows interlayer relaxations of three uniquely terminated surfaces as compared to available experimental studies. Surface relaxations shown in Fe_(s+1)-O_(s)-Fe_(s-1)- are in qualitative agreement with the literature,⁵⁰ which confirms that our models are sufficiently accurate to simulate the iron oxide oxygen carrier.

3.2 CH₄ oxidation on the stoichiometric α -Fe₂O₃(001) surface

The chemical looping reactors include a fuel reactor where the iron oxide oxygen carriers are reduced by reaction with the

methane and an air reactor where the reduced iron oxides are regenerated by re-oxidization with air. Therefore, we assume that there is no oxygen vacancy on the surface of initial iron oxide after being regenerated by re-oxidization with air. The stoichiometric α -Fe₂O₃(001) surface with Fe_(s+1)-O_(s)-Fe_(s-1)- termination can represent the initial surface of the iron oxide oxygen carrier in the CH₄ oxidation process.

To study the CH₄ oxidation process, we first examined the adsorption of CH₄ on the stoichiometric α -Fe₂O₃(001) surface with Fe_(s+1)-O_(s)-Fe_(s-1)- termination. Various adsorption configurations were considered and calculated. In the most favorable case, CH₄ adsorbs at the surface iron Fe_(s+1) site with an adsorption energy of 0.06 eV. We further examined the adsorption of CH_x radicals. Methyl (CH₃) is the first intermediate during CH₄ dehydrogenation. It was found that the C atom of CH₃ directly bonding to the surface iron Fe_(s+1) site is the most stable configuration and the corresponding adsorption energy is 0.32 eV. For the adsorption of methylene (CH₂) radicals, it showed strong affinity towards both the surface iron Fe_(s+1) site and the surface oxygen site. The adsorption energies were 1.26 eV and 1.23 eV, respectively. For the methine (CH) radical, calculations on various adsorption configurations indicated that C-Fe_(s+1) binding is the most stable and the adsorption energy is 2.82 eV. The surface oxygen atop site adsorption is relatively unstable with an adsorption energy of 1.89 eV. For the C radicals, the adsorption energies are 4.84 eV while they bind to the surface Fe_(s+1) site, 5.13 eV to the surface O site, and 4.51 eV to the Fe_(s+1)-O bridge site, which indicates the strong interaction between the C radical and the stoichiometric α -Fe₂O₃(001) surface.

We now examine each of the elementary reactions for CH₄ dehydrogenation and oxidation on the stoichiometric α -Fe₂O₃(001) surface, by starting from CH₄ adsorbed at the Fe atop site. While determining the reaction pathway, we consider all possible intermediates using a three-step approach: (1) all likely H or CH_x binding sites for a new given intermediate were first examined, (2) all possible reaction paths to the given intermediates were calculated, and the low barrier reaction channels were chosen as the means to reach the next intermediates, and thus the competing paths with higher reaction barriers are not discussed further, and (3) the previous two steps are repeated in succession until CO or CO₂ is produced. For example, in the step of CH₃ radical dehydrogenation, all possible final states are considered and two favorable paths are shown in Fig. 2(A). The energy barrier indicates that the H atom from CH₃ dehydrogenation prefers the neighboring surface O site which has not been occupied by the first H atom from CH₄ dehydrogenation. The energy barrier for the formation of final state FS2 with two O-H bonds *via* the 2(O-H) path is 1.52 eV, which is 0.22 eV lower than the barrier for the formation of FS1 *via* the O-2H path where the two dehydrogenated H atoms bind to the same surface oxygen site. Therefore, the 2(O-H) path is chosen as the means to reach the next intermediate. We also consider the CH_x radical evolution by binding with the surface oxygen site. When the adsorbed CH₂ radical migrates from the Fe_(s+1) site to the surface oxygen site, it forms a CH₂O species as shown

Table 1 Surface energy of Fe₂O₃ with various terminations and interlayer relaxations

Surface termination	Surface energy (J m ⁻²)	Interlayer relaxations (%)			
		Fe _(s+1)	O _(s)	Fe _(s-1)	Fe _(s-2)
Fe _(s+1) -O _(s) -Fe _(s-1) -	1.24	38 31*	8 2*	9 5*	6 3*
O _(s) -Fe _(s-1) -Fe _(s-2) -	2.21	—	48 64*	54 62*	38 33*
Fe _(s-1) -Fe _(s-2) -O _(s-3) -	4.15	—	—	36	28

The interlayer relaxation values with * are from experimental results.⁴⁷

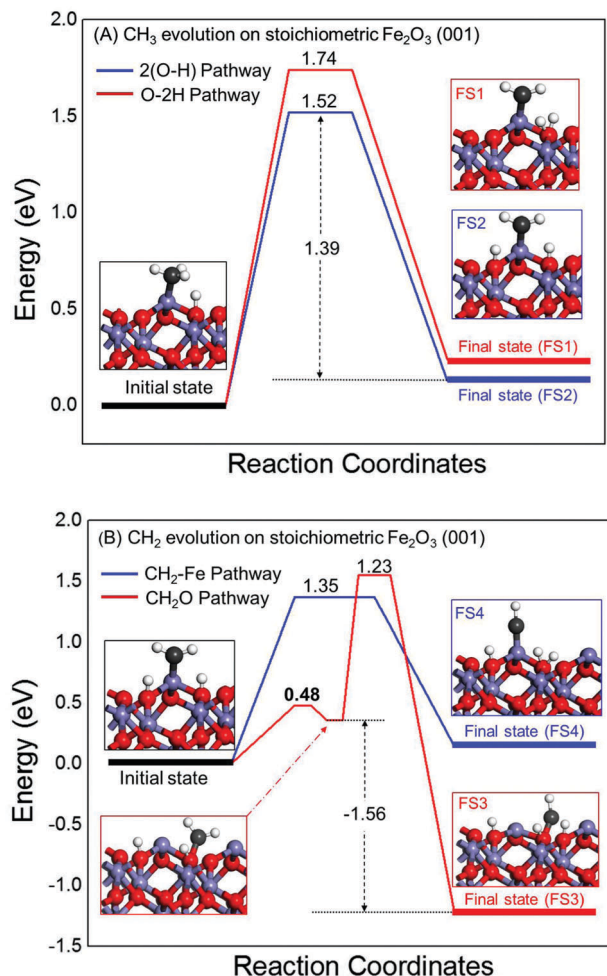


Fig. 2 Determining the pathway of CH₄ oxidation on the stoichiometric α -Fe₂O₃(001) surface using the free energy diagram of CH₃ and CH₂ radical evolution.

in Fig. 2(B). Although the barrier of CH₂O dehydrogenation forming CHO and H, 1.39 eV, is close to the barrier of direct dehydrogenation of CH₂ on the Fe site (1.35 eV), this step is extremely exothermic (−1.36 eV), which makes it unfavorable in the high temperature chemical looping process. The CH₂–Fe path is thus chosen as the means to reach the next intermediate in CH₄ oxidation. Following this approach, the initial CH₄ oxidation mechanism on the stoichiometric α -Fe₂O₃(001) surface with the activation barrier for each elementary step is obtained as shown in Fig. 3. It can be seen that CO₂ and H₂O are produced by CH₄ interaction with lattice oxygen atoms, which indicates that it is CH₄ complete oxidation. The product CO₂ release will result in two oxygen vacancies in the outermost layer of the α -Fe₂O₃(001) surface.

3.3 Vacancy-induced lattice oxygen diffusion

CH₄ oxidation on the stoichiometric α -Fe₂O₃(001) surface creates two surface oxygen vacancies as shown in Fig. 3. We herein consider the most plausible pathways of lattice oxygen diffusion to surface oxygen vacancies and evaluate their diffusion barriers which were calculated using CI-NEB. Stable positions of Fe and O

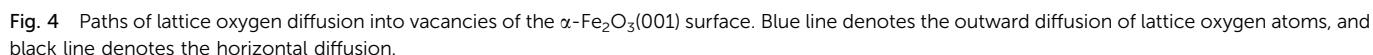
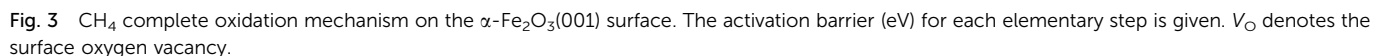
atoms corresponding to local energy minima have been identified through atomic relaxation after two surface oxygen vacancies are introduced at the original site due to CO₂ formation. The diffusion energy barrier is defined as the energy difference between the local minima and the transition state corresponding to the highest energy level along the lattice oxygen diffusion pathway.

First, we study the diffusion of one lattice oxygen atom to heal one surface oxygen vacancy. The two surface oxygen vacancies are labeled as $V_{O(1)}$ and $V_{O(2)}$. From the subsurface to the surface, six distinguishable lattice oxygen atoms are chosen to describe the diffusion pathway for $V_{O(1)}$ healing as shown in Fig. 4. These lattice oxygen atoms are labeled as $O_{(s)A}$, $O_{(s)B}$ and $O_{(s)C}$ in the top layer, and $O_{(s-3)A}$, $O_{(s-3)B}$ and $O_{(s-3)C}$ in the subsurface. For $O_{(s)A}$, $O_{(s)B}$ and $O_{(s)C}$ in the top layer, they can heal the surface vacancy $V_{O(1)}$ via horizontal diffusion, and then create a new surface oxygen vacancy in their original location. For $O_{(s-3)A}$, $O_{(s-3)B}$ and $O_{(s-3)C}$ on the subsurface, they diffuse to the surface vacancy $V_{O(1)}$ through a gap between the corner-sharing and the edge-sharing FeO₆ octahedrons. This oxygen diffusion from the subsurface to the outermost surface leads to the formation of one Fe_(s-1)–O bond and two Fe_(s+1)–O bonds, meanwhile creates one subsurface oxygen vacancy. The calculated diffusion barriers are shown in Fig. 5. From Fig. 5, we can see that the diffusion of lattice oxygen $O_{(s-3)B}$ on the subsurface to $V_{O(1)}$ is the most favorable, with a diffusion barrier of 0.38 eV. Also, it can be seen that the energy barriers for $O_{(s)A}$, $O_{(s)B}$ and $O_{(s)C}$ diffusion are higher than those for $O_{(s-3)A}$, $O_{(s-3)B}$ and $O_{(s-3)C}$ diffusion, which indicates that the outward diffusion of lattice oxygen atoms is more favorable than horizontal diffusion on the same layer. In addition, we found that the vacancy migration from the outermost layer to the subsurface is endothermic, which is in agreement with our previous results that the oxygen vacancy on the top surface of α -Fe₂O₃(001) is more stable than the vacancy on the subsurface.

3.4 CH₄ oxidation on the α -Fe₂O₃(001) surface with oxygen vacancies

Vacancies are created due to CO₂ release during initial CH₄ oxidation on the stoichiometric α -Fe₂O₃(001) surface. Here we further examined the CH₄ oxidation on the α -Fe₂O₃(001) surface with oxygen vacancies $V_{O(2)}$ and $V_{O(s-3)B}$, which have been proved to preferentially form after initial CH₄ oxidation.

We found that the vacancy site is unfavorable for CH₄ adsorption, while the neighboring Fe_(s+1) site has a weak interaction with CH₄, with an adsorption energy of 0.02 eV. For the CH₃ radical, the strongest adsorption configuration resides at the oxygen vacancy site with an adsorption energy of 2.12 eV, which is 1.8 eV higher than the strongest adsorption on the stoichiometric surface. For adsorption of CH₂, the adsorption on the Fe_(s+1) atop site and the vacancy site is found to be nearly identically stable with an adsorption energy of 3.54 eV and 3.58 eV, respectively. The adsorption energy of the most stable CH₂ adsorption configuration on the surface with a $V_{O(1)}$ vacancy is 2.32 eV higher than that on the stoichiometric surface. The influence of vacancies on the CH₂ radicals adsorption is similar to CH₃ radicals. The adsorption strength in both the Fe_(s+1) site and the vacancy shows



results in an increase in the adsorption energy by about 0.01–0.04 eV for CH_x species adsorption. Therefore, the van der Waals interaction should not significantly affect the adsorption of CH_x species. This is because the adsorption of CH_x species is quite strong, and thus, dispersive forces play only a small role.

To determine the CH₄ oxidation reaction pathway on α -Fe₂O₃(001) surfaces with oxygen vacancies, again we use the three-step approach to seek for the most favorable intermediates. Upon the first step of CH₄ dehydrogenation on the Fe_(s+1) site with a neighboring surface oxygen vacancy, the formed CH₃ radical may react with Fe₂O₃ *via* the O-H path where CH₃ remains on the Fe_(s+1) site while the H atom migrates to

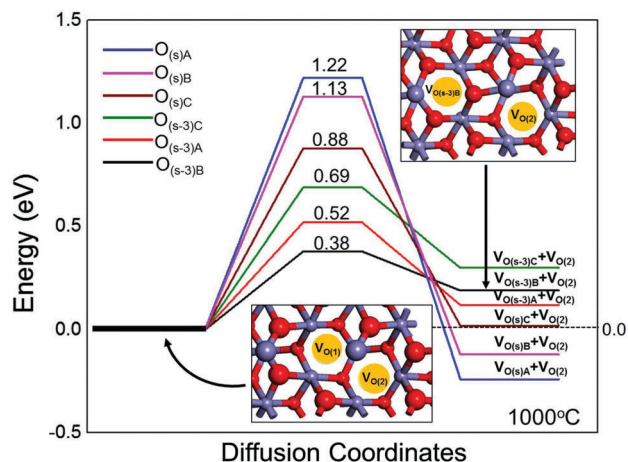


Fig. 5 Energy barrier of lattice oxygen atom outward diffusion ($\text{O}_{(s-3)A}$, $\text{O}_{(s-3)B}$ and $\text{O}_{(s-3)C}$) and horizontal diffusion ($\text{O}_{(s)A}$, $\text{O}_{(s)B}$ and $\text{O}_{(s)C}$) to the surface vacancy of $\alpha\text{-Fe}_2\text{O}_3(001)$.

the surface oxygen site, or *via* the Fe–H path where the CH_3 radical is adsorbed to the neighboring oxygen vacancy site, whereas H remains on the original Fe adsorption site. The calculation shows that the Fe–H path is more favorable with a barrier of 1.72 eV, which is 0.22 eV lower than the barrier of the O–H path as shown in Fig. 6(A). Therefore FS5 is chosen as the intermediate for the following oxidation process. It was found that the C–H bonds of CH_3 are successively cleaved at this vacancy site, and the protons are adsorbed onto the neighboring Fe sites. For the adsorbed CH radical, we also examined the possible O site binding. If CH migrates to the neighboring surface oxygen site, it will form a CHO complex. From Fig. 6(B), we can see that the CHO path needs to overcome a higher barrier (1.55 eV if all H atoms bind to Fe sites and 1.41 eV if one H atom binds to the surface oxygen site) than the CH-V_O path (1.33 eV). Therefore, the CHO path is excluded from the reaction network.

Once an Fe site has two H atoms, a covalent bond is formed between the two H atoms which leads to the formation of a H_2 molecule. After the last C–H bond is cleaved, the lattice oxygen diffuses from the subsurface to the surface vacancy site, to form a C–O complex. The C–O complex transfers to the neighboring Fe site, from which it dissociates as a gaseous CO molecule. This pathway results in partial oxidation of methane. The mechanism is described in Fig. 7. Compared with the mechanism of complete oxidation of methane shown in Fig. 3, we can see that the oxygen vacancies greatly affect CH_4 evolution which leads to syngas production.

Based on the proposed mechanism, we can predict that CO_2 and H_2O are produced in the beginning of oxidation of CH_4 because the initial iron oxide oxygen carrier has been fully oxidized in the air reactor resulting in the adsorption of CH_4 molecules onto the Fe atop sites with no neighboring vacancies and causing subsequent reactions to proceed *via* a complete oxidation pathway. Monazam *et al.*⁵¹ used thermogravimetric analysis to investigate the reduction of Fe_2O_3 in a methane atmosphere over the range of $700\text{--}825^\circ\text{C}$ with a continuous stream of CH_4 (15%, 20%, and 35%), and found that most of

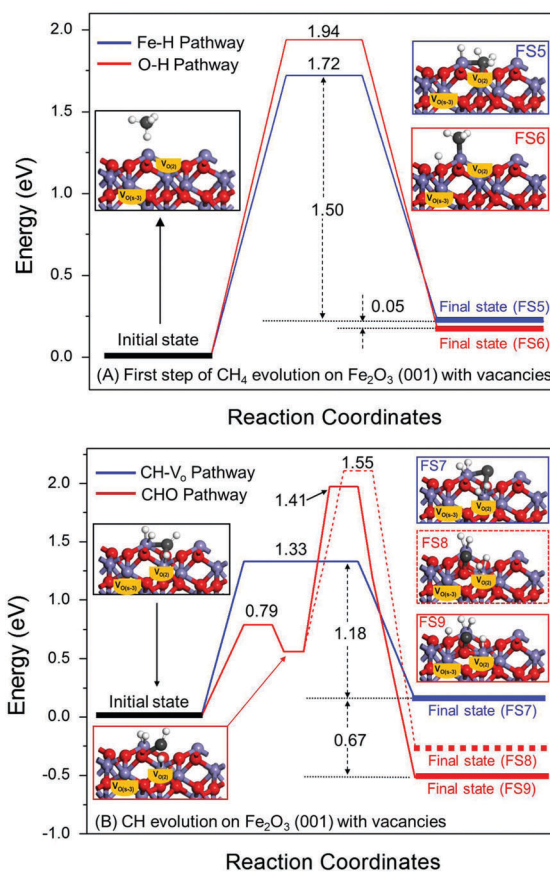


Fig. 6 Determining the pathway of CH_4 oxidation on the reduced $\alpha\text{-Fe}_2\text{O}_3(001)$ surface with oxygen vacancies using the free energy diagram of adsorbed CH_4 and CH radical evolution.

the CH_4 molecules were completely oxidized to CO_2 and H_2O at the early stages of the reduction period, and then CO and H_2 were released due to partial oxidation of CH_4 , which is also in good agreement with our proposed mechanism.

3.5 Oxygen vacancy concentration effect

We have found that oxygen vacancies play an essential role in CH_4 partial oxidation. Here we further investigated the effect of oxygen vacancy concentration on CH_4 oxidation. By removing a 3-fold bridging oxygen (O_{3c}), a vacancy on the top surface $\text{V}_{\text{O}(1)}$ can be created. It results in one 2-fold coordinated Fe (Fe_{2c}) and two 5-fold coordinated Fe (Fe_{5c}). When the third oxygen vacancy is created in our model system including 286 oxygen atoms, the vacancy concentration is about 1%. Similarly, we can create more oxygen vacancies to simulate the reduced $\alpha\text{-Fe}_2\text{O}_3(001)$ surface with higher oxygen vacancy concentration. The distance between neighboring surface vacancies is about 5 Å. We plot the relationship between C–H bond activation energy and oxygen vacancy concentration of $\alpha\text{-Fe}_2\text{O}_3(001)$ in Fig. 8. We can see that the activation barrier of the C–H bond in CH_4 decreases to 1.42 eV from 1.96 eV when the oxygen vacancy concentration increases to about 2.5%, and then remains almost unchanged even though more oxygen vacancies are created. For the activation barrier of the C–H bond in the CH_3 radical, it decreases to

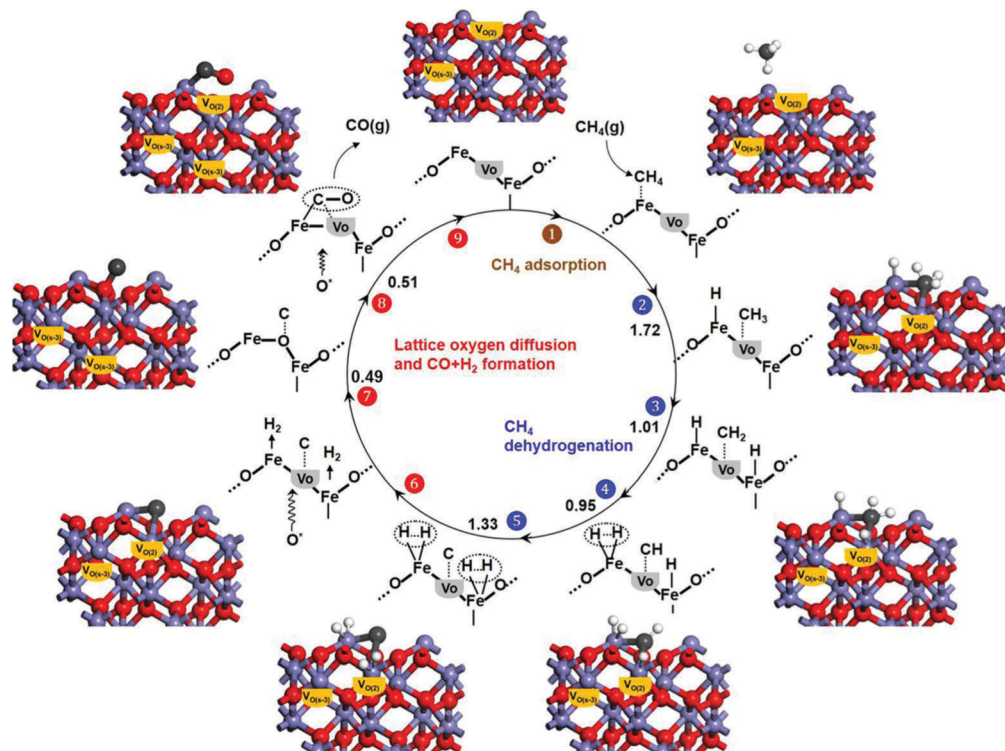


Fig. 7 CH_4 partial oxidation mechanism on the $\alpha\text{-Fe}_2\text{O}_3(001)$ surface with oxygen vacancies. The activation barrier (eV) for each elementary step is given. V_O denotes the surface oxygen vacancy.

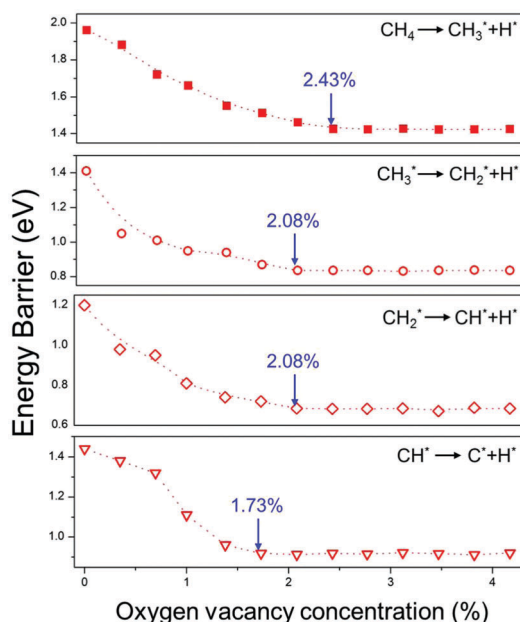


Fig. 8 The relationship between the C–H bond activation energy and the oxygen vacancy concentration of the $\alpha\text{-Fe}_2\text{O}_3(001)$ surface.

0.83 eV from 1.41 eV when the oxygen vacancy concentration increases to about 2%, and then remains at 0.83 eV. A similar trend is observed in the activation of the C–H bond in CH_2 , the lowest barrier is obtained when the oxygen vacancy concentration reaches about 2%. For the activation of the C–H bond in

the CH radical, the lowest barrier is about 0.91 eV and the corresponding oxygen vacancy concentration is 1.73%. These results indicate that increasing oxygen vacancy concentration causes the decrease in the barrier of C–H bond activation, namely, a higher activity for CH_4 partial oxidation. However, when oxygen vacancy concentration is higher than certain values, increasing the oxygen vacancy concentration cannot continue to lower the C–H bond activation barrier. It may be because of the weak interaction between oxygen vacancies in the deeper subsurface and the adsorbed surface species.

To verify the vacancy concentration effect on the kinetics of CH_4 oxidation, we performed a TGA test. The conversion of the sample in TGA, calculated using the following equation, is shown as the black solid line in Fig. 9.

$$X = \frac{(m_b - m_i)M_{\text{Fe}_2\text{O}_3}}{m_b \times 3M_{\text{O}}} \times 100\% \quad (8)$$

where X is the conversion of the iron oxide in TGA. m_b means the beginning weight of the iron oxide in TGA. m_i represents the instant weight in TGA. And $M_{\text{Fe}_2\text{O}_3}$ and M_{O} represent the relative molar mass of Fe_2O_3 and O, respectively. Meanwhile, since the conversion is only related to oxygen, it approximately equals the vacancy concentration in iron oxide. We found that the disaggregated Fe_2O_3 pellet began to agglomerate after about 100 s of heating at 1000 °C due to the sintering effect, so we only examine the reaction between 0 and 100 s, which can represent the early stage of CH_4 oxidation.

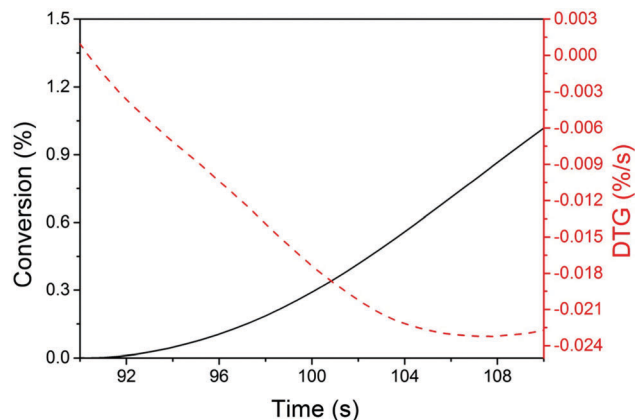


Fig. 9 The TGA results of the iron oxide reacted with methane at 1000 °C.

And the differential TGA (DTG), which represents the reaction rate, is obtained by original TGA weight differential shown as the red dashed line. Fig. 9 shows the immediate weight decrease as soon as methane injection in TGA at 1000 °C. In detail, the differential of the weight decreases promptly in the first stage, meaning the augment of the reaction rate of methane oxidation on iron oxide. This corresponds to the fact that the increase in oxygen vacancy concentration during CH₄ oxidation lowers the barriers of the CH₄ oxidation process. However, when the conversion further increases, the reaction rate remains identical, which is in qualitative agreement with our conclusion that the barrier of CH₄ oxidation cannot further decrease when the oxygen vacancy concentration reaches a certain value.

From Fig. 7 and 8, we can see that the first step of CH₄ dehydrogenation is the rate-limiting step of CH₄ partial oxidation, and the lowest barrier is obtained at an oxygen vacancy concentration of 2.43%. Therefore, we plotted the energy profile of CH₄ partial oxidation on the surface with about 2.5% oxygen concentration as shown in Fig. 10. For comparison, the energy profile of CH₄ complete oxidation is also plotted in Fig. 10.

We can see that the barriers of CH₄ hydrogenation are higher than the barriers of lattice oxygen diffusion in both the partial oxidation and the complete oxidation of methane. In addition, it clearly shows that 2.5% oxygen vacancies can lower 0.5–0.6 eV barriers in the CH₄ dehydrogenation process which greatly facilitates CH₄ activation. 2.5% oxygen vacancies also lower about 0.15 eV of cleavage energy of the Fe–C bond, slightly facilitating CH₄ oxidation in the second stage. For the complete oxidation of methane, the highest barrier is 1.96 eV while it is 1.42 eV for the partial oxidation of methane. They both are within the range of the reported experimental values (150–270 kJ mol^{−1}).⁵² We have found an inert support TiO₂ previously, which can lower the vacancy formation energy, and thus can lead to oxygen vacancy formation.⁵³ Therefore, we can increase the activity of oxygen carriers by adding suitable inert support materials and increase CLPO efficiency by adjusting the suitable methane oxidation time in the chemical looping cycle.

4. Conclusion

Ab initio DFT+*U* calculations and experimental studies on complete oxidation of methane to CO₂ and H₂O, and partial oxidation of methane to syngas on iron oxide oxygen carriers were carried out to elucidate the reaction mechanism and the oxygen vacancy effects on the reactivity of oxygen carriers. We found that Fe_(s+1)–O_(s)–Fe_(s−1) is the dominant termination of the α-Fe₂O₃(001) surface at 1000 °C, and the oxygen vacancy prefers to form on the top surface with this termination. CH_x species interacts with lattice oxygen on the stoichiometric surface leading to CH₄ complete oxidation with the formation of CO₂ and H₂O, as well as surface vacancies. The lattice oxygen atoms prefer outward diffusion to heal the surface vacancies instead of horizontal diffusion on the same layer. In the presence of oxygen vacancies on the top surface and the subsurface, methyl (CH₃) dehydrogenated from CH₄ binds to the vacancy

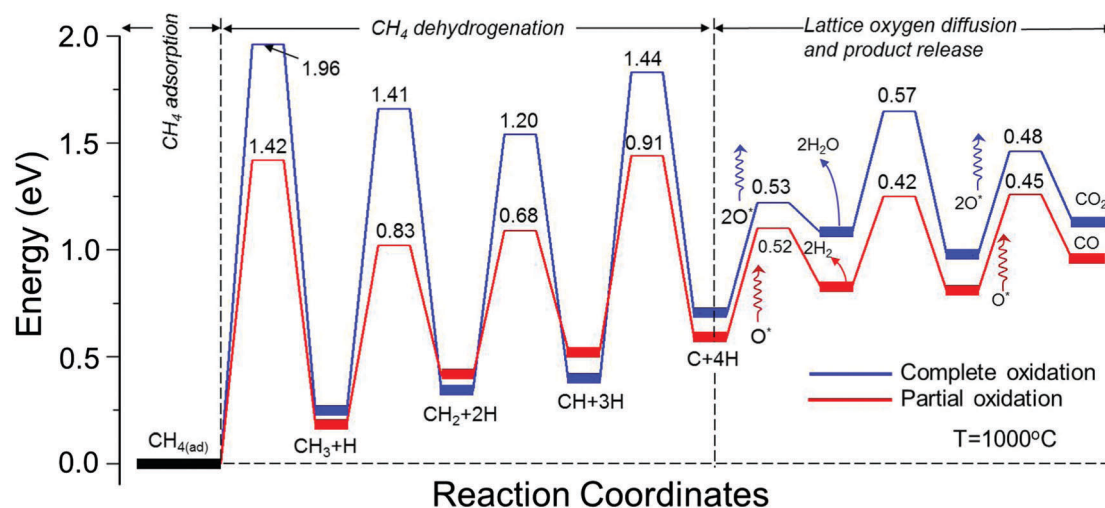


Fig. 10 CH₄ oxidation energy profile through complete oxidation and partial oxidation on the α-Fe₂O₃(001) surface with 2.5% oxygen vacancies.

site and evolves into CO and H₂. The increase in oxygen vacancy concentration will facilitate the CH₄ partial oxidation by lowering the activation barriers of C–H bonds and the cleavage energy of the Fe–C bond. However, when the oxygen vacancy concentration is higher than 2.5%, increasing the oxygen vacancy concentration cannot continue to lower the oxidation barriers. Based on the vacancy effect on the oxidation process and the intermediate examination, the energy profile of partial oxidation of methane to syngas promoted by oxygen vacancies was proposed. We found that the CH₄ initial dehydrogenation into CH₃ radicals is the rate-limiting step of both the partial oxidation pathway and the complete oxidation pathway. In the beginning of oxidation of CH₄, CO₂ and H₂O will be produced because the initial iron oxide oxygen carrier has been fully oxidized in the air reactor resulting in CH₄ molecules that are adsorbed onto the Fe atop sites with no neighboring vacancies and the subsequent reactions will proceed *via* the complete oxidation pathway and create oxygen vacancies, and then the CO and H₂ can be produced by partial oxidation with these oxygen vacancies. These findings based on the proposed mechanism are in good agreement with the results obtained by the TGA test. The fundamental insight into the oxygen vacancy promoted CH₄ partial oxidation on iron oxide oxygen carriers can be applied to design and develop more efficient metal oxide systems and reaction conditions in a wide variety of chemical looping applications.

Acknowledgements

The valuable support provided by the Supercomputer Center at The Ohio State University is gratefully acknowledged.

References

- 1 L.-S. Fan, L. Zeng and S. Luo, *AIChE J.*, 2015, **61**, 2–22.
- 2 S. Bhavsar, M. Najera, R. Solunke and G. Veser, *Catal. Today*, 2014, **228**, 96–105.
- 3 K. Li, H. Wang and Y. Wei, *J. Chem.*, 2013, 1–8.
- 4 A. Tong, D. Sridhar, Z. Sun, H. R. Kim, L. Zeng, F. Wang, D. Wang, M. V. Kathe, S. Luo, Z. Sun and L.-S. Fan, *Fuel*, 2013, **103**, 495–505.
- 5 F. He, Y. Wei, H. Li and H. Wang, *Energy Fuels*, 2009, **23**, 2095.
- 6 F. Li, R. Kim, D. Sridhar, F. Wang, L. Zeng, J. Chen and L.-S. Fan, *Energy Fuels*, 2009, **23**, 4182–4189.
- 7 L. F. de Diego, M. Ortiz, J. Adánez, F. García-Labiano, A. Abad and P. Gayán, *Chem. Eng. J.*, 2008, **144**, 289–298.
- 8 G. Azimi, T. Mattisson, H. Leion, M. Rydén and A. Lyngfelt, *Int. J. Greenhouse Gas Control*, 2015, **34**, 12–24.
- 9 T. Kodama, H. Ohtake, S. Matsumoto, A. Aoki, T. Shimizu and Y. Kitayama, *Energy*, 2000, **25**, 411–425.
- 10 A. Abad, F. García-Labiano, L. F. de Diego, P. Gayán and J. Adánez, *Energy Fuels*, 2007, **21**, 1843–1853.
- 11 J. Adánez, L. F. de Diego, F. García-Labiano, P. Gayán, A. Abad and J. M. Palacios, *Energy Fuels*, 2004, **18**, 371.
- 12 L.-S. Fan, *Chemical Looping Systems for Fossil Energy Conversions*, John Wiley & Sons, Hoboken, NJ, 2010.
- 13 T. Mattisson, A. Lyngfelt and P. Cho, *Fuel*, 2001, **80**, 1953–1962.
- 14 S. Luo, L. Zeng, D. Xu, M. Kathe, E. Chung, N. Deshpande, L. Qin, A. Majumder, T.-L. Hsieh, A. Tong, Z. Sun and L.-S. Fan, *Energy Environ. Sci.*, 2014, **7**, 4104–4117.
- 15 Y. Jin, C. Sun and S. Su, *Phys. Chem. Chem. Phys.*, 2015, **17**, 16277.
- 16 L. Huang, M. Tang, M. Fan and H. Cheng, *Appl. Energy*, 2015, **159**, 132–144.
- 17 Z. Cheng, L. Qin, M. Guo, J. A. Fan, D. Xu and L.-S. Fan, *Phys. Chem. Chem. Phys.*, 2016, **18**, 16423–16435.
- 18 N. H. Linha, T. Q. Nguyena, W. A. Diñoa and H. Kasa, *Surf. Sci.*, 2015, **633**, 38–45.
- 19 Y. X. Pan, C. J. Liu, D. Mei and Q. Ge, *Langmuir*, 2010, **26**, 5551–5558.
- 20 Z. Cheng, B. J. Sherman and C. S. Lo, *J. Chem. Phys.*, 2013, **138**, 014702.
- 21 A. Kiejna, *Phys. Rev. B: Condens. Matter Mater. Phys.*, 2003, **68**, 235405.
- 22 Z. Cheng and C. Lo, *Phys. Chem. Chem. Phys.*, 2016, **18**, 7987–7996.
- 23 I. Goikoetxea, M. Alducin, R. Díez Muiñoab and J. I. Juaristiab, *Phys. Chem. Chem. Phys.*, 2012, **14**, 7471–7480.
- 24 R. M. Van Natter, J. S. Coleman and C. R. F. Lund, *J. Mol. Catal. A: Chem.*, 2008, **292**, 76–82.
- 25 Z. Cheng and C. S. Lo, *ACS Catal.*, 2012, **2**, 341–349.
- 26 R. O. Jones, *Rev. Mod. Phys.*, 2015, **87**, 897.
- 27 O. Warschkow, D. E. Ellis, J. Hwang, N. Mansourian-Hadavi and T. O. Mason, *J. Am. Ceram. Soc.*, 2002, **85**, 213–220.
- 28 P. Wanaguru, J. An and Q. Zhang, *Appl. Phys.*, 2016, **119**, 084302.
- 29 H. Ueta, L. Chen, R. D. Beck, I. Colón-Díaz and B. Jackson, *Phys. Chem. Chem. Phys.*, 2013, **15**, 20526–20535.
- 30 Z. Cheng and C. Lo, *Ind. Eng. Chem. Res.*, 2013, **52**, 15447–15454.
- 31 X. Shen, Z. Zhang and D. H. Zhang, *Phys. Chem. Chem. Phys.*, 2015, **17**, 25499–25504.
- 32 Z. Cheng, N. Fine and C. Lo, *Top. Catal.*, 2012, **55**, 345–352.
- 33 G. Kresse and J. Hafner, *Phys. Rev. B: Condens. Matter Mater. Phys.*, 1993, **47**, 558.
- 34 G. Kresse and J. Furthmuller, *Comput. Mater. Sci.*, 1996, **6**, 15.
- 35 G. Kresse and J. Furthmuller, *Phys. Rev. B: Condens. Matter Mater. Phys.*, 1996, **54**, 11169.
- 36 J. P. Perdew, K. Burke and M. Ernzerhof, *Phys. Rev. Lett.*, 1996, **77**, 3865.
- 37 P. E. Blöchl, *Phys. Rev. B: Condens. Matter Mater. Phys.*, 1994, **50**, 17953.
- 38 G. Kresse and D. Joubert, *Phys. Rev. B: Condens. Matter Mater. Phys.*, 1999, **59**, 1758.
- 39 P. E. Blöchl, O. Jepsen and O. K. Anderson, *Phys. Rev. B: Condens. Matter Mater. Phys.*, 1994, 16223.
- 40 J. F. Herbst, R. E. Watson and J. W. Wilkins, *Phys. Rev. B: Condens. Matter Mater. Phys.*, 1978, **17**, 3089.

- 41 V. I. Anisimov and O. Gunnarsson, *Phys. Rev. B: Condens. Matter Mater. Phys.*, 1991, **43**, 7570.
- 42 X. Huang, S. K. Ramadugu and S. E. Mason, *J. Phys. Chem. C*, 2016, **120**, 4919–4930.
- 43 G. Rollmann, A. Rohrbach, P. Entel and J. Hafner, *Phys. Rev. B: Condens. Matter Mater. Phys.*, 2004, **69**, 165107.
- 44 R. L. Blake, R. E. Hessevic, T. Zoltai and L. W. Finger, *Am. Mineral.*, 1966, **51**, 123.
- 45 N. J. Mosey, P. Liao and E. A. Carter, *J. Chem. Phys.*, 2008, **129**, 014103.
- 46 D. Sheppard and G. Henkelman, *J. Comput. Chem.*, 2011, **32**, 1769–1771.
- 47 G. Henkelman, B. P. Uberuaga and H. J. Jonsson, *J. Chem. Phys.*, 2000, **113**, 9901.
- 48 Z. Cheng and C. S. Lo, *ACS Catal.*, 2015, **5**, 59–72.
- 49 M. Lübke and W. Moritz, *J. Phys.: Condens. Matter*, 2009, **21**, 134010.
- 50 R. L. Kurtz and V. E. Henrich, *Surf. Sci.*, 1983, **129**, 345–354.
- 51 E. R. Monazam, R. W. Breault, R. Siriwardane, G. Richards and S. Carpenter, *Chem. Eng. J.*, 2013, **232**, 478–487.
- 52 D. Ghosh, A. K. Roy and A. Ghosh, *Trans. Iron Steel Inst. Jpn.*, 1986, **26**, 186–193.
- 53 L. Qin, Z. Cheng, J. A. Fan, D. Kopechek, D. Xu, N. Deshpande and L.-S. Fan, *J. Mater. Chem. A*, 2015, **3**, 11302–11312.